Methyl Ester Functionalized Phenalenyl Arene- and Bipyridine-ruthenium Based Complexes for Electroactive Langmuir-Blodgett Films

Isis Mani Wahl[a], Eduard Westphal[b], Tiago Leyser da Costa Gouveia[a†], Francielli Sousa Santana[a], David L. Hughes[c], Ronny R. Ribeiro[a], Leonardo Henrique Ribeiro Piccoli[a], Herbert Winnischofer[a]*.

[a]Departamento de Química, Universidade Federal do Paraná, 81530-900, Curitiba-PR, Brazil.

[b]Departamento Acadêmico de Química e Biologia, Universidade Tecnológica Federal do Paraná, 81280-340, Curitiba-PR, Brazil.

[c]School of Chemistry, University of East Anglia, Norwich NR4 7TJ, United Kingdom.

ABSTRACT. We report the synthesis of a new phenalenyl ligand, functionalized with a methyl ester electron withdrawing group, named 9-hydroxy-1-oxo-1*H*-phenalen-5-methyl carboxylate (**L**) and the generated complexes [Ru(bpy)$_2$**L**]PF$_6$ and [(η^6-C$_6$H$_6$)Ru(**L**)Cl]. Compounds were characterized by spectroscopic and X-ray diffraction methods and their electrochemical behavior was investigated via cyclic voltammetry and UV-vis spectroelectrochemistry. The one-electron oxidized compounds have unpaired electron located in the phenalenyl ring, as supported by theoretical calculations (DFT) and EPR results. Langmuir-Blodgett (LB) films deposited by [Ru(bpy)$_2$**L**]$^{2+/3+}$ species mixed with stearic acid are electroactive, showing quasi-reversible

wave with $E_{1/2}^{Film\ 1} = 0.74$ V and $E_{1/2}^{Film\ 2} = 0.81$, which are promising systems that allows the access to immobilized open-shell species in the film.

INTRODUCTION. The unique chemistry of ruthenium has boosted a large development of structurally diverse ruthenium complexes in the last decades.[1,2] These complexes can be found in works that range from photochemical[3], photophysical and electrochemical[3] studies to catalytic[4] and antitumor applications[5]. To reach such a wide range of applications, the selection of the ligands is the crucial point in the design of ruthenium complexes. In this sense, many studies use the strategy of a well-established class of ruthenium compounds as the basis for the design of new complexes, making modifications in ancillary ligands in order to reach new properties and improve existing ones.[6–8] Therefore, the search for new ancillary ligands is one of the central themes in developing new bipyridyl and η^6-arene ruthenium complexes. With this in mind, one class of ligands that has been drawing attention is the multicyclic phenalenyl (PLY) based ligands.[9,10,19,11–18]

PLY based ligands are generally found in the chelate form with O,O-, N,O-, and N,N-donor atoms.[10] The complexes with these ligands are able to transition between closed-shell and open-shell configurations through, for example, electron transfer in redox processes.[9,10] Their interesting electronic properties give them a non-innocent character which can be exploited in the design of new coordination compounds.[9,10] One interesting PLY derivative is 9-hydroxyphenalenone, since it can generate chelate complexes through its oxygens, being already investigated in compounds with cytotoxic activity[13], electrocatalytic properties[9], redox studies with ruthenium complexes[20], molecular spin memory device[17], etc. Despite the relevance

of ruthenium compounds in the context of coordination chemistry, few studies have been developed aimed at association of ruthenium and PLY based ligands.[20,21]

Motivated by the rich chemistry of phenalenyl based compounds, our group designed and synthetized a new PLY-based ligand in which the 5 position of the 9-hydroxyphenalenone is functionalized with an ester group forming a new compound named methyl 9-hydroxy-1-oxo-1H-phenalene-5-carboxylate (**L**) (Figure 1-a). The insertion of an electron withdrawing group, such as an ester, at the 5-position of the 9-hydroxyphenenalenone represents a modification not yet described in the literature, in which the electron density of the PLY is decreased. Besides, the versatility of an ester group allows future structural modifications. Therefore, herein we describe the structural and electronic characterization of the ligand and two new ruthenium complexes, [Ru(bpy)$_2$**L**]PF$_6$ (bpy = bipyridine) and [(η^6-C$_6$H$_6$)Ru(**L**)Cl] (Figure 1-b and 1-c). Density functional theory (DFT) calculations were performed to support the interpretations. We also describe the construction and study of Langmuir-Blodgett (LB) films with the [Ru(bpy)$_2$**L**]PF$_6$ complex, in two distinct oxidation states: Ru^{II} and Ru^{III} named **Film 1** and **Film 2.** These films were prepared using a mixture of the complex with stearic acid. LB films have the advantage of allowing the construction of films with a high degree of orientation, allied also to precise thickness control.[22,23]
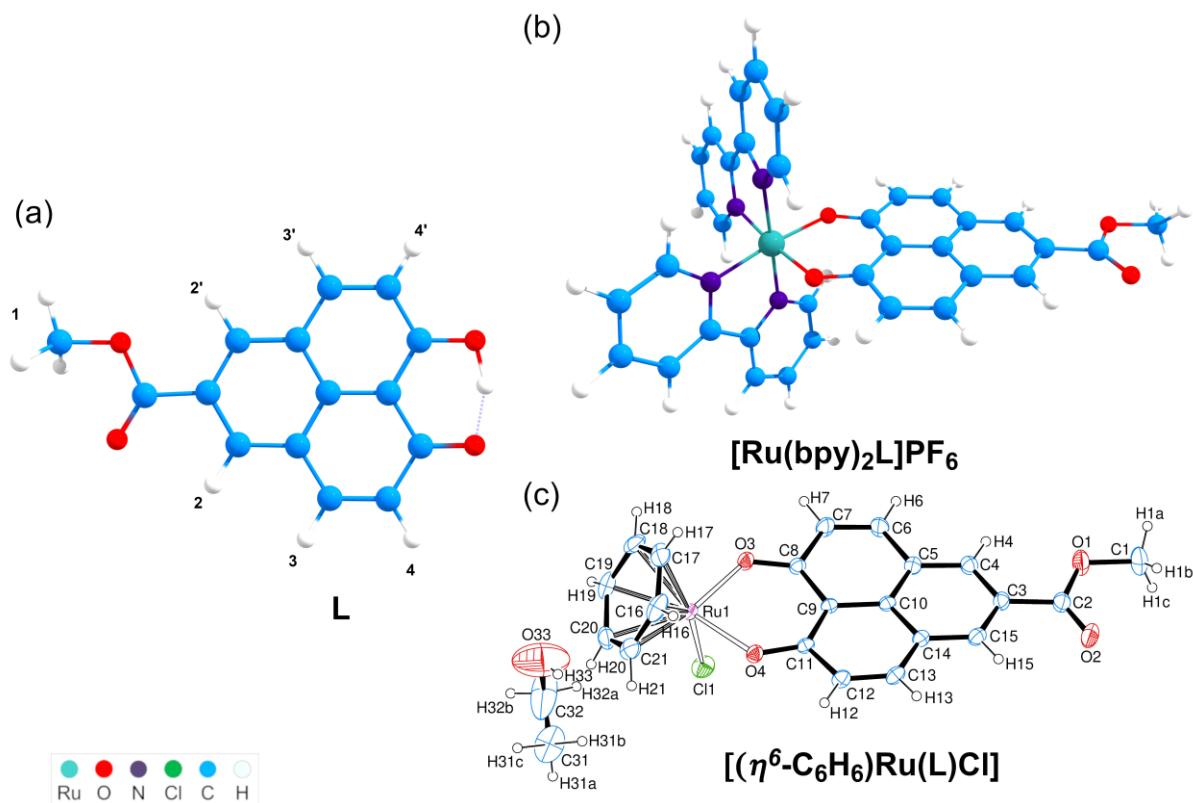
Figure 1. DFT optimized geometries for (a) **L** and (b) [Ru(bpy)$_2$**L**]PF$_6$; (c) an ORTEP plot of [(η^6-C$_6$H$_6$)Ru(**L**)Cl] with ellipsoids drawn at 50% probability.

RESULTS AND DISCUSSION. The proposed **L** ligand as well as the complexes [Ru(bpy)$_2$**L**]PF$_6$ and [(η^6-C$_6$H$_6$)Ru(**L**)Cl] were successfully synthesized as described below. **L** was prepared adapting the method described by Haddon,[24] in which methyl 6-methoxy-2-naphthoate was reacted with freshly prepared cinnamoyl chloride and excess aluminum chloride in 1,2-dichloroethane. As illustrated in Scheme 1, this reaction occurs in two steps in a one-pot synthesis: the first addition of AlCl$_3$ promotes the Friedel–Crafts acylation to form the intermediate methyl 5-cinnamoyl-6-methoxynaphthalene-2-carboxylate. The second addition of AlCl$_3$ promotes the demethylation followed by an intramolecular Michael addition and the elimination of the phenyl ring.[25] The complexes [Ru(bpy)$_2$**L**]PF$_6$ and [(η^6-C$_6$H$_6$)Ru(**L**)Cl] were

4

synthesized from the precursors [Ru(bpy)$_2$Cl$_2$] and [{(η^6-C$_6$H$_6$)RuCl}$_2$Cl$_2$], respectively, mixed with a solution of **L** and NEt$_3$ (Scheme 2).
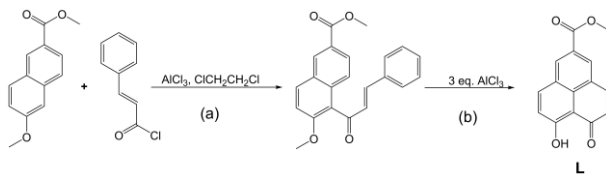
Scheme 1. Synthetic route for **L** composed of a (a) Friedel-Crafts acylation, (b) a demethylation of the hydroxyl group, an acid catalyzed intramolecular Michael addition, and the elimination of an acid catalyzed phenyl group.
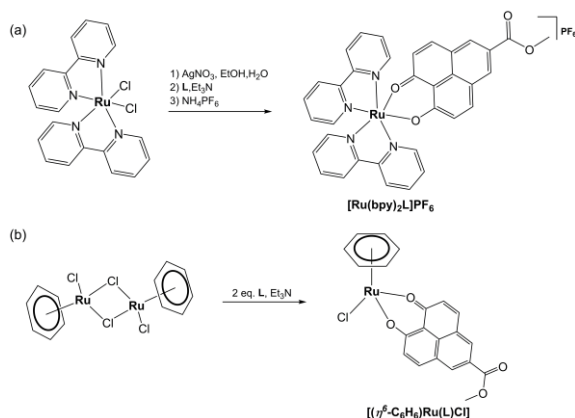
Scheme 2. Synthetic route for the complexes (a) [Ru(bpy)$_2$**L**]PF$_6$ and (b) [(η^6-C$_6$H$_6$)Ru(**L**)Cl].

NMR spectroscopy. Ligand **L** and the complexes [Ru(bpy)$_2$**L**]PF$_6$ and [(η^6-C$_6$H$_6$)Ru(**L**)Cl were characterized by ^{1}H NMR spectroscopy in solutions of CDCl$_3$ and DMSO-d_6; some selected signals are shown in Table 1. The **L** spectra (Figure S1) show 3 signals related to the aromatic hydrogens between 9-7 ppm. The singlet signal at 3.98 ppm indicates the presence of the ester group, while the phenol hydrogen can be observed at 16.28 ppm due to intramolecular hydrogen bonding. In the spectra of both complexes (Figures S3 and S5), the **L** signals shift and the phenol signal disappears, which indicate the coordination of **L**. All signals

relating to the hydrogens of ligand **L** are shifted to lower frequencies (higher field region) compared to those of the free ligand. This indicates an increase in the electron density on these hydrogens, which evidences the π-acceptor character of **L**.

Table 1. Selected ^{1}H NMR data of **L** and the complexes.

Assignment	**L**^{a}		$[(\eta^6$-C$_6$H$_6)$Ru(**L**)Cl]^b		**[Ru(bpy)$_2$L]PF$_6$**^{a}	
	δ / ppm		δ / ppm		δ / ppm	
OH	16.28	s, 1H	-	-	-	-
1	3.98	s, 3H	3.98	s, 3H	3.93	s, 3H
2,2'	8.90	s, 2H	8.46	s, 2H	8.65	s, 2H
3,3'	8.61	d, 2H (J = 9.3 Hz)	7.84	d, 2H (J = 9.3 Hz)	8.12	d, 2H (J = 9.2 Hz)
4,4'	7.33	d, 2H (J = 9.3 Hz)	7.21	d, 2H (J = 9.3 Hz)	6.96	d, 2H (J = 9.2 Hz)

Solution of ^{a}DMSO-d_6; ^{b}CDCl$_3$

Crystal Structure. Crystals of the $[(\eta^6$-C$_6$H$_6)$Ru(**L**)Cl] complex were obtained from the recrystallization of the material in ethanol. The structure, determined from X-ray diffraction methods, is shown in the ORTEP diagram for the complex in Figure 1-c; selected bond distances and angles can be found in Table 2. The complete molecular dimensions are in the Supplementary Material. The complex presented pseudo-octahedral geometry, in which the arene ligand occupies three coordination positions, consistent with that expected for the "piano stool" complex type. The ligand **L** binds to the ruthenium atom with a bite angle of 87.09(6)°, forming a 6-membered ring. The complex showed π-stacking intermolecular interactions between the rings of the ligand **L**, about a center of symmetry; the rings are *ca* 3.50 Å apart, with a distance between the centroids of rings at 3.679 Å (Figure S16). The $[(\eta^6$-C$_6$H$_6)$Ru(**L**)Cl] complex showed Ru(1)–Cl(1) (2.4116(6) Å) and Ru–C (C = centroid; Figure S16) (1.653 Å) binding distances comparable with Ru^{II}-arene complexes found in the literature.[26] On the other hand, the values found for Ru(1)–O(3) and Ru(1)–O(4) bonds of 2.0540(16) and 2.0534(15) Å, respectively, are similar and slightly smaller than that typically found for Ru^{II}–arene complexes

containing β-diketonated ligands, as for example acetylacetonate (~2.07 Å). This is in agreement with the shortening promoted by a resonance structure.[7,27]

Table 2. Selected bond distances and bond angles of $[(\eta^6\text{-}C_6H_6)Ru(\mathbf{L})Cl]$.

Bond distance (Å)		Bond angle (°)	
Ru-O(3)	2.0534(15)	O(4)-Ru(1)-O(3)	87.09(6)
Ru-O(4)	2.0540(16)	O(4)-Ru(1)-Cl(1)	85.58(5)
Ru-Cl	2.4116(6)	O(3)-Ru(1)-Cl(1)	84.12(5)
Ru-C(centroid)	1.6531	C(centroid)-Ru-O(4)	126.56
O(4)-C(11)	1.277(3)	C(centroid)-Ru-O(3)	129.48
O(3)-C(8)	1.278(3)	C(centroid)-Ru-Cl	128.92

Attempts were also made to crystallize complex $[Ru(bpy)_2\mathbf{L}]PF_6$; these, however, resulted in low quality crystals (data not shown in this work). Despite obtaining crystallographic data that are not suitable for publication, it was possible to confirm the proposed structure for $[Ru(bpy)_2\mathbf{L}]PF_6$ (Figure S17).

Electrochemical Studies. The electrochemical studies were performed through cyclic voltammetry (CV) (Figure 2 and Table 3) and UV-vis spectroelectrochemistry experiments (Figure 3 and Figure S7). The acquired electrochemical results were analyzed and are discussed using DFT calculation data.
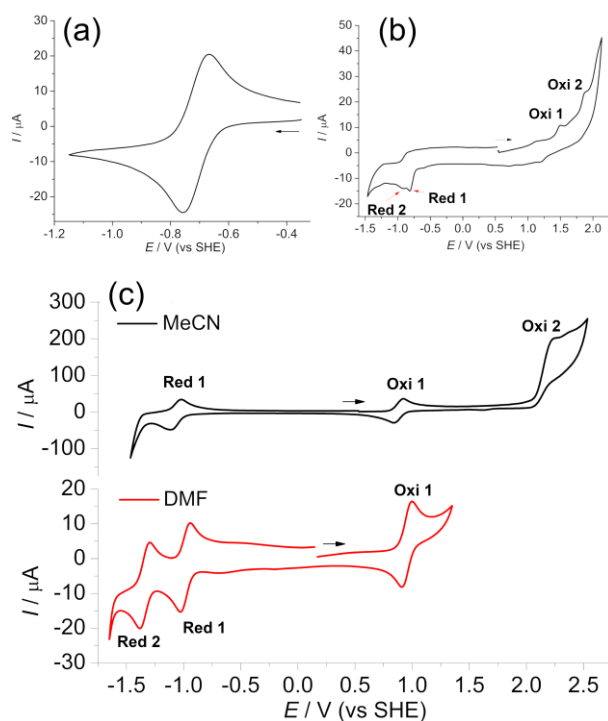
Figure 2. Cyclic voltammograms of (a) ligand **L** in DMF, (b) complex $[(\eta^6\text{-}C_6H_6)Ru(\mathbf{L})Cl]$ in acetonitrile and (c) $[Ru(bpy)_2\mathbf{L}]PF_6$ in acetonitrile and DMF. Solutions were prepared in TBAClO$_4$ 0.1 mol L^{-1}. All voltammograms show the first cycle at scan rates of 100 mV s^{-1}.

Table 3. Electrochemical data extracted from CV for **L**, $[Ru(bpy)_2\mathbf{L}]PF_6$ and $[(\eta^6\text{-}C_6H_6)Ru(\mathbf{L})Cl]$.

Compound	$E_{1/2}^{red2}$ / V	$E_{1/2}^{red1}$ / V	$E_{1/2}^{oxi1}$ / V	E_{pa}^{oxi2} / V
L	-	-0.71	-	-
$[Ru(bpy)_2\mathbf{L}]PF_6$	-1.34[a]	-0.98[a]	0.88[b]	2.24[b]*
$[(\eta^6\text{-}C_6H_6)Ru(\mathbf{L})Cl]$	-0.91*	-0.81*	1.50*	1.88*

Potential values extracted from CV in DMF[a] or acetonitrile[b]; *irreversible processes

Methyl 9-hydroxy-1-oxo-1*H*-phenalene-5-carboxylate (L). The CV of **L** showed only one reversible redox pair in the potential window analyzed (1.35 V to -1.65 V vs SHE). DFT calculations were performed to obtain the molecular orbitals (MOs) of **L** in its neutral and

reduced state (Figure S8 and S9). The energies of the MOs of the reduced ligand are higher compared to the neutral form, which causes a destabilization of the MOs. DFT data reveals that the π^* LUMO orbital is delocalized on the molecule, involving aromatic rings and oxo and hydroxyl groups.

The value of the reduction potential found for **L** ligand is less negative than for other polycyclic species and it does not present a second reduction process. This may be due to the great destabilization of MOs when the reduction occurs. The LUMO orbital of **L** has energy of -2.95 eV, while the reduced ligand (**L$^\bullet$**) has a SOMO with energy of -0.42 eV, in which reduction occurs below the lower potential limit of the electrolyte solution.

UV-vis spectroelectrochemistry: The reduction of **L** leads to the bathochromic shift of all bands and the intensification of two bands at 289 nm and 300 nm (Figure S7). When **L** is reduced, the SOMO-LUMO energy gap decreases, thus the other virtual orbitals (LUMO+1α and β, LUMO+2α and β) are also closer to the energy of the SOMO orbital (Figure S8 and S9). This approximation in the energy of the filled orbitals with the virtual orbitals leads to less energetic transitions, explaining the bathochromic shift observed.

[(η^6-C$_6$H$_6$)Ru(L)Cl]. The CV of the complex [(η^6-C$_6$H$_6$)Ru(**L**)Cl], performed in acetonitrile (Figure 2-b), shows four irreversible Faradaic processes, two oxidation ($E_{pa}^{oxi1} = 1.50$ V and $E_{pa}^{oxi1} = 1.88$ V) and two reduction ($E_{pc}^{red1} = -0.815$ V and $E_{pc}^{red2} = -0.915$ V). The analysis of the MOs (Table 4, Figure S10 to S12) supports the CV results. All the MOs that depart from the observed redox processes have a higher contribution of **L**.

In neutral form, [(η^6-C$_6$H$_6$)Ru(**L**)Cl] HOMO orbital has a 52.6% contribution of the **L** bonding orbitals, thereby the first oxidation occurs on **L**. The HOMO orbital energy of **L** (-6.80

eV) is lower than the HOMO orbital energy of the complex $[(\eta^6\text{-}C_6H_6)Ru(\mathbf{L})Cl]$ (-5.99 eV). This explains why this oxidation was not observed in the potential window analyzed. The second oxidation process can also be attributed to the oxidation of $\mathbf{L}$ since the SOMO orbital of $[(\eta^6\text{-}C_6H_6)Ru(\mathbf{L})Cl]^+$ has 81.7 % $\mathbf{L}$ contribution.

The LUMO orbital of the complex $[(\eta^6\text{-}C_6H_6)Ru(\mathbf{L})Cl]$ is 96.2% $\mathbf{L}$ centered, therefore the reduction wave at $E_{pc}{}^{red1}$ = -0.815 V is attributed to a reduction localized on $\mathbf{L}$. This process occurs in a more negative potential than the free ligand ($E_{1/2}$ = -0.713 V) and this can be explained by the higher energy (-2.72 eV) of the complex LUMO orbital than the free ligand (-2.95 eV) LUMO orbital. In addition, the first reduction is irreversible in the $[(\eta^6\text{-}C_6H_6)Ru(\mathbf{L})Cl]$, in contrast to that observed in the free $\mathbf{L}$. The complex has a second reduction process that differs from the free ligand. This reduction also occurs on $\mathbf{L}$ since the SOMO orbital has 93.4% contribution of $\mathbf{L}$.

Table 4. Fragment contribution and energy for each molecular orbital of $[(\eta^6\text{-}C_6H_6)Ru(\mathbf{L})Cl]^{-/0/+}$

	Orbital	Ru / %	L / %	arene / %	Cl / %	Energy / eV
$[(\eta^6\text{-}C_6H_6)Ru(\mathbf{L})Cl]^-$	SOMO	4.1	93.4	2.5	0.0	-0.69
$[(\eta^6\text{-}C_6H_6)Ru(\mathbf{L})Cl]$	LUMO	1.7	96.2	2.0	0.0	-2.72
	HOMO	23.7	52.6	9.6	14.1	-5.99
$[(\eta^6\text{-}C_6H_6)Ru(\mathbf{L})Cl]^+$	SOMO	9.5	81.7	3.4	5.5	-9.74

[Ru(bpy)$_2$L]PF$_6$. The CV of the complex [Ru(bpy)$_2$**L**]PF$_6$ was performed in acetonitrile and in *N,N*-dimethylformamide (DMF) (Figure 2-c). The CV in acetonitrile solution shows three electrochemical processes, two reversible, $E_{1/2}{}^{red1}$ = -1.06 V and $E_{1/2}{}^{oxi1}$ = 0.88 V, and one irreversible, $E_a{}^{oxi2}$ = 2.24 V, whilst the CV in DMF solution shows three reversible electrochemical processes, at $E_{1/2}{}^{red2}$ = -1.34 V, $E_{1/2}{}^{red1}$ = -0.98 V and $E_{1/2}{}^{oxi1}$ = 0.95 V.

The HOMO orbital of $[Ru^{II}(bpy)_2L]^+$ has a higher contribution of ruthenium atom, 44.5%, (Table 5), consistent with the first oxidation assigned to $Ru^{III/II}$ process. Das et al. made the same assignment for the analogous complex $[Ru(bpy)_2(O,O-PLY)]ClO_4^{21}$ with $E_{1/2}{}^{oxi1} = 0.74$ V vs SHE (original value converted from SCE by adding +0.244 V).[21,28] However, it is important to note that HOMO has also a high **L** contribution (43.8%). The second oxidation process (E^{oxi2}) is an irreversible process visible only in acetonitrile solution. The SOMO orbital of the oxidized complex $[Ru(bpy)_2\mathbf{L}]^{2+}$ (Table 5) is centered on the ligand **L** (90.9% contribution), so the second oxidation process was attributed to the oxidation of the **L** ligand. This assignment differs from that provided by Das et al. which suggest that this process also has the contribution of the $Ru^{III} \rightarrow Ru^{IV}$.[21]

The LUMO orbital of $[Ru^{II}(bpy)_2\mathbf{L}]^+$ is centered on the bipyridine ligand, thus the first reduction process (E^{red1}) is bipyridine centered. The second reduction process (E^{red2}) is only visible in DMF solution. The reduced complex $[Ru^{II}(bpy)_2\mathbf{L}]^0$ has the SOMO orbital centered on the bipyridine ligand (Table 5); the second reduction process occurs on the second bipyridine. The DFT calculations is consistent with assignments found in the literature.[21,29,30] The reduction of **L** is not seen since only the LUMO+2 orbital has **L** character.

The Lever electrochemical parameter for **L** (E_L = -0.078 V) is similar to other O-donors such as acetylacetonate (-0.08) and o-acetylphenolate (-0.07)[31], confirming that **L** has predominantly donor character. The $E_{1/2}{}^{oxi1}$ of $[Ru(bpy)_2\mathbf{L}]PF_6$ ($E_{1/2}{}^{oxi1}$ = 0.883 V) is a result of the electron donation by **L** to the metallic center, which stabilizes the ruthenium in the highest oxidation state (Ru^{III}). From the point of view of MOs, a higher electron density on the metal destabilizes the HOMO orbital.

The analogous $[Ru(bpy)_2(O,O\text{-}PLY)]ClO_4$[21] complex shows a slightly lower $E_{1/2}{}^{oxi1}$ than that of $[Ru(bpy)_2\mathbf{L}]PF_6$. This difference is explained by the presence of the ester group in the ancillary ligand which removes electron density from the rings and results in a weaker donor than 9-oxyphenenalenone (O,O-PLY).

UV-vis spectroelectrochemistry. Figure 3 shows the spectral changes observed in the UV-vis spectroelectrochemical experiments. Figure 3-a corresponds to the $Ru^{II}{\rightarrow}Ru^{III}$ oxidation process. The intensity of the band at $bpy(\pi^*) \leftarrow Ru\ (\pi)$ and $\mathbf{L}(\pi^*) \leftarrow Ru\ (\pi)$ MLCT at 517 nm decreases with concomitant increases in the intensity at d-d and $Ru^{III}(d\pi){\leftarrow}\mathbf{L}^-(\pi)$ LMCT at 757 nm.[21] The $bpy(\pi^*{\leftarrow}\ \pi)$ band at 296 nm decreases in intensity and unfolds in two bands at 280 nm and 313 nm. Figure 3-b shows the spectral changes related to the first reduction process $(bpy)^{0/-}$. The bands related bipyridine ligand decrease: 518 nm (MLTC) and 296 nm ($\pi^* \leftarrow \pi$). Figure 3-c shows the spectral changes related to $\mathbf{L}$ oxidation process. As discussed above, this process proved to be irreversible and all bands vanish with the applied potential. Similar profile was reported by Das et al.[21]

Table 5. Fragment contribution and energy for each molecular orbital of $[Ru(bpy)_2\mathbf{L}]^{0/+/2+}$

	Orbital	**Ru / %**	**L / %**	**bpy 1 / %**	**bpy 2 / %**	**Energy / eV**
$[Ru(bpy)_2\mathbf{L}]^0$	SOMO	4.9	17.5	38.8	38.8	-3.08
$[Ru(bpy)_2\mathbf{L}]^+$	LUMO	6.6	6.6	46.0	40.9	-4.86
	HOMO	44.5	43.8	6.1	5.6	-7.99
$[Ru(bpy)_2\mathbf{L}]^{2+}$	SOMO	6.8	90.9	0.9	1.3	-11.36

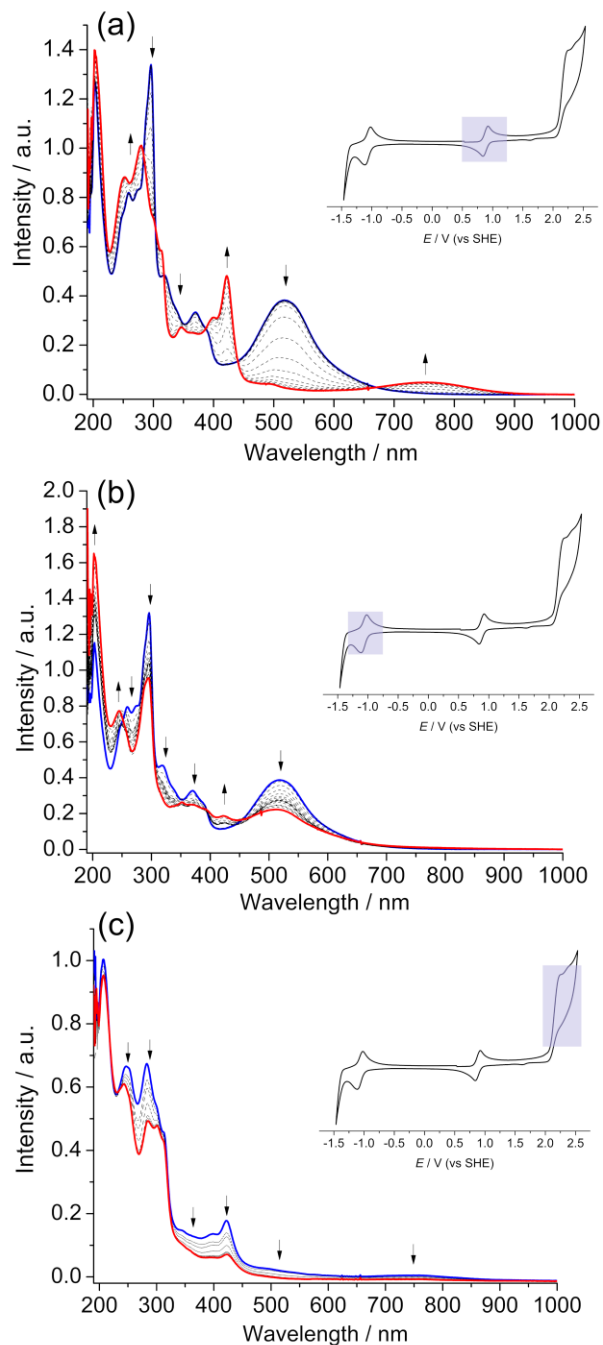**Figure 3.** Spectroelectrochemistry of [Ru(bpy)$_2$**L**]PF$_6$ showing the spectral changes related to redox processes (a) Oxi 1, (b) Red 1 and (c) Oxi 2. The arrows indicate the changes related to the oxidation processes (a) and (c), and the reduction process (b). The experiment was performed in TBAClO$_4$ 0.1 mol L^{-1} acetonitrile solution.

EPR spectroscopy. Figure 4 shows the 77 K EPR spectrum recorded from frozen acetonitrile solution of [Ru(bpy)$_2$**L**]PF$_6$ with a small amount of hydrogen peroxide and of hydrochloric acid, along the simulation of a S = ½ spin system representative of a mononuclear low spin Ru^{III} species. The reaction with hydrogen peroxide can lead to three different spin species. (i) The major species is a low spin S = ½ Ru^{III} species formed by the oxidation of the metal on the original complex, which presence is marked by the simulation. The principal values of the simulated g-tensor, g$_x$ = 2.632, g$_y$ = 2.239 and g$_z$ = 1.587 (g$_{iso}$ = 2.156) are in accordance to the rhombic coordination structure demonstrated by crystallography (Figure S17). (ii) An unpaired electron stabilized on the **L** ligand[21], the radical species assigned on Figure 4, represents the second statistically relevant entity. (iii) The simultaneous occurrence of the former and the latter in a single molecular unit gives rise to the third species, also statistically relevant. This species is the magnetic result of the weak exchange interaction between the unpaired electron on the **L** ligand and the unpaired electron of the low spin Ru^{III} center. The magnetic coupling hence leads to an effective S = 1 spin system, in which energy frame the $\Delta m_S = \pm 2$ Half Field Transition (~1550 G) occurs as an unmistakable sign of magnetic coupling between spin species.
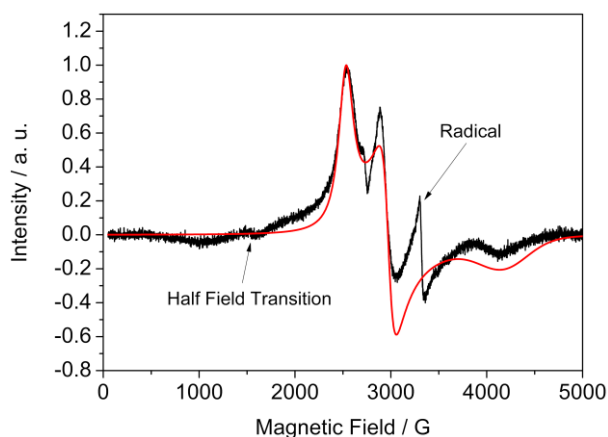
Figure 4. Frozen acetonitrile solution of $[Ru(bpy)_2L]PF_6$ with a small amount H_2O_2 and HCl 77 K EPR spectrum (black line) and simulation (red line). The radical resonance is due to an unpaired electron on the ligand **L** and the Half Field Transition is the telltale sign of the magnetic coupling between this electron and the Ru^{III} unpaired electron.

Langmuir-Blodgett mixed films. Langmuir and Langmuir-Blodgett films were prepared using the redox reversible species $[Ru(bpy)_2L]PF_6$ mixed with stearic acid $(CH_3(CH_2)_{16}COOH)$ in a ratio of 1:1. Generally, LB films are generated using amphiphilic molecules, since the amphiphilic character confers the ability to self-organize at the liquid-air interface. However, $[Ru(bpy)_2L]PF_6$ alone is not suitable to deposit LB films since it does not form stable monolayers due to considerable solubility in the aqueous subphase at the experimental conditions. The use of stearic acid mixed with $[Ru(bpy)_2L]PF_6$ serve as a strategy for deposition since it stabilizes the monolayer at the liquid-air interface.[32–35] The Langmuir films were assembled with complexes in two distinct oxidation states, Ru^{II} and Ru^{III}, and the films were named **Film 1** and **Film 2**, respectively. The oxidized species was generated by the reaction with hydrogen peroxide and hydrochloric acid (see experimental section).

Before the deposition of the films, the time-stability of the monolayers was evaluated by monitoring the change of area at a given time (3300 s) at constant pressure, 33 mN.m^{-1} for **Film 1** and 28 mN.m^{-1} for **Film 2** (Figure S18). The films presented a loss of mass of 12.3% and 6.60% for **Film 1** and **Film 2,** respectively. This loss probably reflects the ability of complex molecules diffuse into the aqueous phase, even then, the film was considered stable enough for deposition on solid substrates.

15

Π-A isotherm. The Π-A isotherms for **Film 1** and **Film 2** are shown in Figure 5. In both films, inflection changes can be observed in the curves associated to phase transitions. The transition to the liquid state occurs around 85 Å^2 for the **Film 1** and 60 Å^2 for **Film 2**. The liquid state extends to around 31 Å^2 in the **Film 1** and 35 Å^2 for the **Film 2**. **Film 1** exhibited an additional transition within the liquid phase region around 55 Å^2. This is probably due to a change in arrangement of the molecules. The transition for the solid state was about 33 mN m^{-1} and 28 mN m^{-1} for **Film 1** and **Film 2**, respectively, so these values of Π were chosen for the depositions of the LB films. The molecular areas (*A*) found in both films were very similar, 42 Å^2 and 43 Å^2, for **Film 1** and **Film 2**, respectively. The *A* value is larger than that normally found for pure stearic acid (20 Å^2), indicating the presence of the complex in the films. On the other hand, the molecular areas found are low compared to the estimated area of the projection of a molecule of the complex (around 100 Å^2), obtained by the DFT calculation. This means that the molecules of the complex are not arranged side by side forming an ideal monolayer, so it is more likely that they overlap in the film arrangement. The collapse for both films occurs around 45 mN m^{-1}, a value lower than that typically found for pure stearic acid film (65 mN m^{-1}).
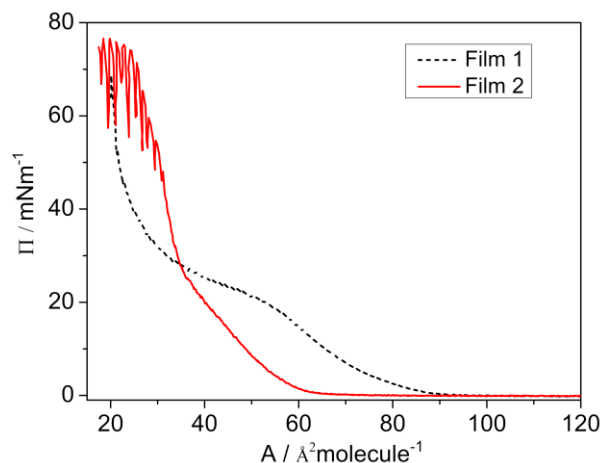
Figure 5. Π–A curves obtained for **Film 1** (black line) and **Film 2** (red line), bar speed: 100 $cm^2\,min^{-1}$

Reflection-Absorption Spectroscopy. For the Infrared Reflection-Absorption Spectroscopy (IRRAS) experiment, the mixed films were deposited on a gold substrate. Figure 6 shows the spectra obtained for **Film 1** and **Film 2**. The IRRAS spectra for the two mixed films evaluated presented the same profile. These spectra mainly revealed bands compatible with the presence of stearic acid. Between 2962 cm^{-1} and 2850 cm^{-1} bands are found referring to C–H stretches of the aliphatic chain. The intense signal at 1704 cm^{-1} is compatible with the C=O stretch in stearic acid. No bands were observed regarding the aromatic C–C stretches of **L** (1623 cm^{-1}), probably because this region of the spectra is covered by the stearic acid bands. Also, no bands of the PF_6^- (838 cm^{-1} and 557 cm^{-1}) counter ion were observed in the film spectra. The absence of the PF_6^- bands may suggest that it is diffusing into the aqueous subphase during deposition of the films and it is replaced by stearate ion as a counter ion. Therefore, the stabilization of the monolayer occurs due to electrostatic interaction between $[Ru^{II}(bpy)_2\mathbf{L}]^{+/2+}$ and stearic anion. However, the 1704 cm^{-1} band of the deposited films is compatible with

(protonated) stearic acid, indicating that the deposited LB films are constituted predominantly by stearic acid molecules, with some $[Ru^{II}(bpy)_2L]$/stearate pairs immobilized.
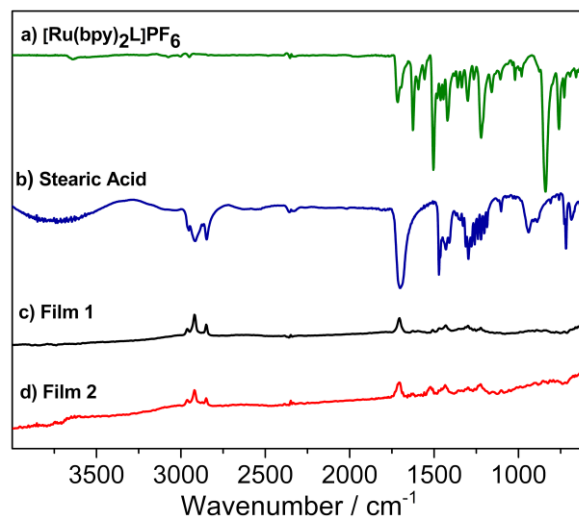

Figure 6. FTIR spectra of the complex (a) $[Ru(bpy)_2L]PF_6$ and (b) stearic acid. Specular reflectance at 80° grazing angle for (c) **Film 1** and (d) **Film 2** deposited at gold substrate. The bands in (a) and (b) face downward and the bands in (c) and (d) face upward for better visualization and comparison.

UV-vis absorption spectroscopy of the LB films. UV-vis absorption spectroscopy was used to characterize **Film 1** and **Film 2** deposited on quartz substrate (Figure 7). The spectra of both films show the same bands found in the solution spectra of the complex and the oxidized complex, which proves the presence of complex in the deposited films. Small changes were observed between the spectrum bands of the films and in solution suggesting a low interaction between the molecules. The most significant change, in addition to the scattering effect at higher frequencies, is the band shift at 258 nm in solution to 245 nm (Δ = -13 nm) for **Film 1**. This behavior may indicate that there is a small interaction between the $[Ru^{II}(bpy)_2L]$ molecules or, more likely, π-stacking between **L** portions in which **L** chromophores interact face-to-face

18

resulting in the small hypsochromic shift observed.[36] The MLCT band has the same maximum at 517 nm in both solution and **Film 1**. These results point to weak interactions indicating considerable space distance between $[Ru^{II}(bpy)_2\mathbf{L}]$ molecules.[37]
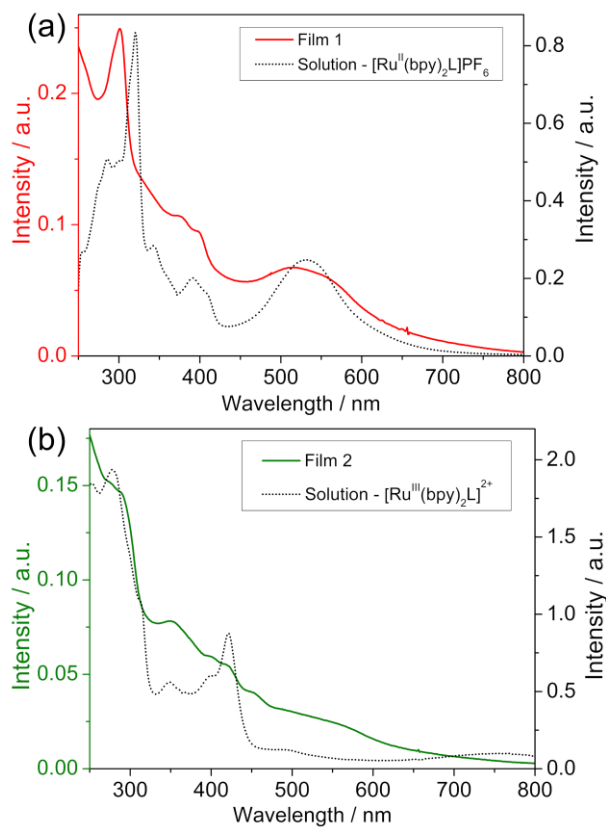

Figure 7. UV-vis spectra of complex $[Ru(bpy)_2\mathbf{L}]PF_6$ in solution of acetonitrile and films on quartz substrate. On the top, (a) spectra in solution of $[Ru^{II}(bpy)_2\mathbf{L}]PF_6$ (black line) and the **Film 1** (red line). In the bottom, (b) spectra in solution of the oxidized complex $[Ru^{III}(bpy)_2\mathbf{L}]^{2+}$ (black line) and **Film 2** (green line).

Cyclic voltammetry of the films. The study of the electrochemical behavior through the cyclic voltammetry of **Film 1** and **Film 2** deposited on a glassy substrate with an FTO conductive layer (Fluorine doped Tin Oxide) is shown in Figure 8.

Film 1 presented a very symmetrical process with slightly distorted bell shape, with $E_{1/2}{}^{Film\ 1} = 0.74$ V. We note that the I_{pa} is almost twice the I_{pc}, which means that not all the oxidized species in the process are reduced to their initial state. On the other hand, **Film 2** presented more symmetrical redox waves, with $E_{1/2}{}^{Film\ 2} = 0.81$, but with ΔEp values more than three times higher than for **Film 1**. The ΔEp values increase with increasing velocity for both films. Figure 8 shows that the diffusion current increases with the scan rates. This indicates that the electron hopping is relatively slow compared to the time of the analysis, resulting in the slightly distorted "bell" shape.

Figure 8 inserts show that both anodic and cathodic Ip are directly proportional to scanning velocity, thus showing that there is no diffusional limitation in the electron transport in the film.
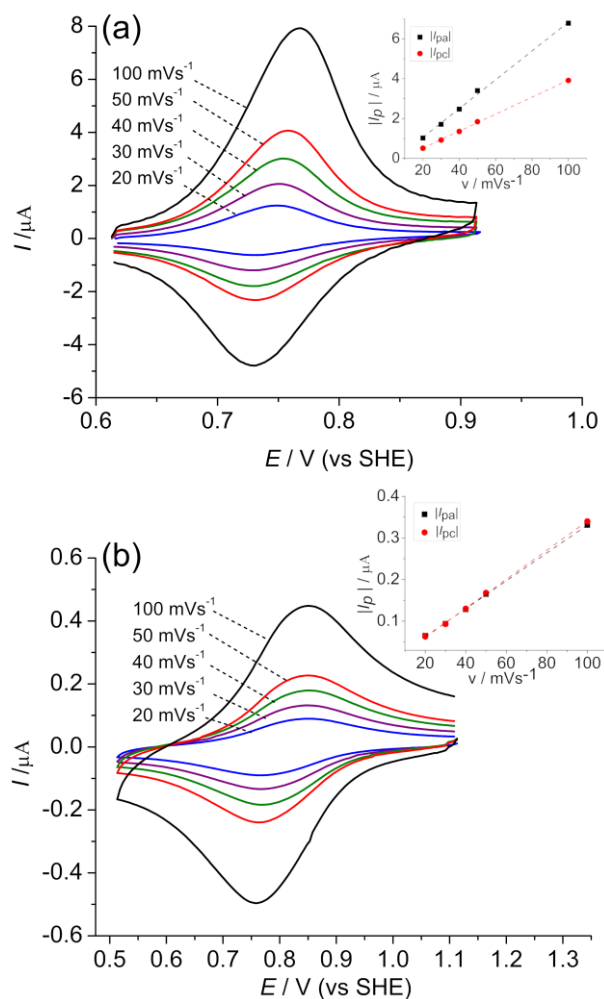
Figure 8. Cyclic voltammograms (CV) of (a) **Film 1** and (b) **Film 2** deposited on FTO substrate. The CVs show scan rates of 20, 30, 40, 50, and 100 mV s^{-1} and the Ip vs v plot for each film.

CONCLUSIONS

The new molecule methyl 9-hydroxy-1-oxo-1H-phenalene-5-carboxylate (**L**) as well as the complexes [Ru(bpy)$_2$**L**]PF$_6$ and [(η^6-C$_6$H$_6$)Ru(**L**)Cl] were successfully synthesized and characterized. Langmuir-Blodgett films were obtained from a mix of [Ru(bpy)$_2$**L**]$^{n+}$ (n = 1 or 2) complex with stearic acid. The Langmuir isotherm studies show the formation of a stable film which was deposited on quartz, gold and FTO substrate. The UV-vis confirms the

immobilization of the complex. The IRRAS suggest that PF_6^- is replaced by the stearate ion and the deposited LB film is constituted mainly by stearic acid molecules with [Ru(bpy)$_2$**L**]/stearate pairs immobilized. The voltammetric experiments of the film show quasi reversible redox waves attributed to the Ru$^{III/II}$ species. According to DFT calculation, the HOMO orbital involved in the oxidation process has 33.9% **L** contribution, indicating the oxidized species generated in the LB films has a Ru^{III} character, but also a radical **L$^+$** character. This property should be interesting to explore in thin films, in particular for future applications that are based on low energy unpaired electrons.

EXPERIMENTAL SECTION

Materials. The reagents and solvents were analytical grade; they were purchased from commercial sources and used as received, except for the acetonitrile and *N,N*-dimethylformamide used in cyclic voltammetry and UV-Vis spectroelectrochemistry, and 1,2-dichloroethane used in the synthetic steps. The acetonitrile was treated with calcium chloride ($CaCl_2$), distilled with calcium hydride (CaH_2) and used immediately, while DMF was dried over-night with 4 Å molecular sieves. The 1,2-dichloroethane was dried using a 3Å molecular sieve. Deionized water used in the LB trough was obtained from the Millipore®Milli-Q system (R = 18.3 MΩ cm), transported in a glass flask and used immediately.

Instrumentation. High-Resolution Mass Spectra were recorded in a Bruker micrOTOF-Q II mass spectrometer, using an APPI ionization source. The ^{1}H and ^{13}C NMR spectra were recorded on a Bruker DPX 200 (4.7 T) or in a Bruker Avance III 400 spectrometer (9.4 T). Deuterated chloroform (CDCl$_3$) or deuterated DMSO (DMSO-d_6) was used as solvent and TMS was used as the internal standard. The IRRAS spectra of the LB films deposited on gold

substrates were registered using a Bruker Vertex 70 spectrophotometer in the range of 4000 to 400 cm^{-1} with the A518/Q specular reflectance at 80 ° with 4 cm^{-1} resolution. UV-vis spectra were obtained from dichloromethane solutions placed in quartz cuvettes and from the LB films deposited on quartz plates using an Agilent 8453 spectrophotometer in the transmission mode. The electrochemical experiments were performed on an Ivium Compactstat potentiostat/galvanostat in a three-electrode cell. For the cyclic voltammetry in solution, the working electrode used was a platinum disc (diameter 3 mm), the reference electrode was Ag/AgNO$_3$ (0.05 mol L^{-1} in acetonitrile) with a platinum wire as counter electrode. Experiments were conducted in 0.1 mol L^{-1} TBAClO$_4$ electrolyte solution in dichloromethane, acetonitrile or DMF (depending on the solubility of the compound). The cyclic voltammetry of the films was carried out in aqueous 0.5 mol L^{-1} KNO$_3$ electrolyte solution, using LB films deposited on FTO which worked as working electrode, Ag/AgCl (NaCl 3 mol L^{-1}) as reference electrode and platinum wire as counter electrode. UV-vis spectroelectrochemistry experiments were conducted using the Ivium Compactstat potentiostat/galvanostat coupled with the HP Agilent 8453 spectrophotometer, and an ALS SEC-C Thin Layer Quartz Glass Spectroelectrochemical cell kit with Pt gauze working electrode. Elemental analysis was carried out with a Perkin-Elmer 2400 elemental analyzer. EPR spectroscopy were performed on a X-band Bruker EMX-micro spectrometer equipped with a quartz insertion finger dewar for liquid nitrogen frozen solution experiments. Spectra were recorded at 9.341792 GHz microwave frequency, 10.0 G of modulation amplitude, 5.12 ms signal channel time constant, 300.0 s sweep time and 5000 spectral points. Simulations were performed using the EasySpin software package.[38] The EPR sample was prepared by dissolving 3 mg of the [Ru(bpy)$_2$Cl$_2$] complex in 1 mL of acetonitrile then adding 2 µL of hydrogen peroxide and 2 µL of hydrochloric acid. The solution was allowed

to react for 10 min, then it was frozen in liquid nitrogen and the EPR measurement was performed.

Experimental

The synthesis of the precursors [{(η^6-C$_6$H$_6$)RuCl}$_2$Cl$_2$ and [Ru(bpy)$_2$Cl$_2$] were prepared according to the reported procedures.[39,40]

Methyl 9-hydroxy-1-oxo-1*H*-phenalene-5-carboxylate (L). The ligand **L** synthesis was based on a modified synthetic procedure for 9-hydroxyphenalenone described by Haddon[24]. This procedure consisted of the reaction of 0.45 g (2.1 mmol) of methyl 6-methoxy-2-naphthoate and 0.35 g (2.1 mmol) of cinnamoyl chloride in 15 mL of dry 1,2-dichloroethane under an argon atmosphere. After complete dissolution of the reactants, the reaction was cooled in an ice bath and 0.28 g (2.10 mmol) of aluminum chloride was added slowly. The reaction was stirred under ice bath for 30 min, then removed from the bath and stirred for another 30 min. A further 0.84 g (6.30 mmol) of aluminum chloride was then added slowly and the reaction was refluxed vigorously (T = 120 °C) under stirring for 14 hours. After this time, the reaction was cooled to room temperature and 20 mL of a dilute hydrochloric acid solution (approximately 5,0 M) was added. The mixture formed was filtered to remove an insoluble black solid material, which was washed with distilled water and dichloromethane. The resulting solution was transferred to a separatory funnel where the aqueous phase was washed with three portions of dichloromethane. The resulting organic phase was evaporated to give a black solid. Purification of this solid was carried out in two steps: first, the separation of the solid by filtration on silica, using dichloromethane as the eluent, resulting in an orange solid after evaporation of the solvent. In the second step, the solid was washed with a small amount of acetonitrile, resulting in 0.37 g of a

yellow solid (33% yield). Q-TOF/MS for $C_{15}H_{11}O_4$ [M+H]$^+$: m/z Calculated: 255.0652; m/z Found: 255.0654. Elemental Anal. Calcd for $C_{15}H_{11}O_4.0.5H_2O$: C, 68.44%; H, 4.21% . Found: C, 68,79%; H, 3.88%; N, 0.06% ^{1}H NMR (CDCl$_3$) δ ppm: 4.04 (s, 3H), 7.23 (d, J = 9.3 Hz, 2H), 8.17 (d, J = 9.3 Hz, 2H), 8.69 (s, 2H), 16.09 (s, 1H). ^{13}C NMR (CDCl$_3$) δ ppm: 52.56; 111.1; 124.68; 125.32; 126.02; 129.35; 133.50; 141.53; 166.35; 179.94. ^{1}H NMR (DMSO-d_6) δ ppm: 3.98 (s, 3H), 7.33 (d, J = 9.4 Hz, 2H), 8.61 (d, J = 9.4 Hz, 2H), 8.90 (s, 2H), 16.28 (s, 1H).

[(η^6-C$_6$H$_6$)Ru(L)Cl]. For the synthesis of the [(η^6-C$_6$H$_6$)Ru(**L**)Cl] complex, 100 mg (0.20 mmol) of the precursor [{(η^6-C$_6$H$_6$)RuCl}$_2$Cl$_2$] was added to a flask containing 50 mL of ethanol. In parallel, a solution containing 98.5 mg (0.39 mmol) of the **L** ligand and 56 μL (0.40 mmol) of triethylamine in 50 mL of ethanol was prepared, and was heated with stirring for 10 minutes, until dissolution. The ligand solution was then slowly transferred to the flask containing the solution of the precursor. The mixture was stirred under reflux for 18 hours. The reddish orange solution formed was evaporated to give an orange solid. This solid was recrystallized from ethanol and washed with excess ice-cold ethanol and ethyl ether. Yield was 10%. Elemental Anal. Calcd for $C_{22}H_{18}ClO_4Ru.2H_2O$: C, 50.06%; H, 3.80%. Found: C, 50.51%; H, 3.64%; N, 0.12%. ^{1}H NMR (CDCl$_3$) δ ppm: 3.98 (s, 3H), 5.75 (s, 6H), 7.21 (d, J = 9.3 Hz, 2H), 7.85 (d, J = 9.3 Hz, 2H), 8.46 (s, 2H). ^{13}C NMR (CDCl$_3$) δ ppm: 52.36; 82.85; 125.17; 128.15; 132.79; 139.05; 177.86.

[Ru(bpy)$_2$L]PF$_6$. For the synthesis of the [Ru(bpy)$_2$**L**]PF$_6$ complex, 100 mg (0.2 mmol) of the precursor Ru(bpy)$_2$Cl$_2$.2H$_2$O and 68 mg (0.4 mmol) of AgNO$_3$ were added in a flask containing 30 mL of an ethanol/water solution (2:1) under argon atmosphere. The reaction was stirred under reflux for 1 hour. After this time, precipitation of AgCl was removed by filtration. In parallel, a solution containing 51 mg (0.2 mmol) of the **L** ligand and 28 μL (0.2 mmol) of

triethylamine in 10 mL of ethanol was prepared. This solution was placed in a flask and, under argon atmosphere, heated under stirring for 10 minutes, until complete dissolution. Then, the filtered solution was added to the ligand solution. The reaction was stirred under reflux for 6 hours. The resulting purple solution was concentrated via evaporation under low pressure and then 2 equivalents of NH_4PF_6 were added. The solution was left for 3 days at room temperature and then filtered. The resulting black solid was dissolved in ice cold acetonitrile, which resulted in an intensely purple solution with a yellow precipitate. The yellow solid was removed by filtration. The solution was rota-evaporated to dryness to give a slightly purple, black solid. This solid was recrystallized from ethanol with excess NH_4PF_6. 89 mg of the $[Ru(bpy)_2L]PF_6$ complex (55% yield) were obtained. Q-TOF/MS for $[Ru(bpy)_2L]^+ = C_{35}H_{25}N_4O_4Ru^+$ $[M]^+$: m/z Calculated: 667.0914; m/z Found: 667.0924. Elemental Anal. Calcd for $C_{35}H_{25}F_6N_4O_4PRu.H_2O$: C, 50.67%; H, 3.28%; N, 6.75%. Found: C, 50.60%; H, 3.26%; N, 6.77%. ^1H NMR (DMSO-d_6) δ ppm: 3.98 (s, 3H), 6.95 (d, J = 9.2 Hz, 2H), 7.30 (t, J = 6.4 Hz, 2H), 7.69 (t, J = 6.0 Hz, 2H), 7.81 (d, J = 5.3 Hz, 2H), 7.94 (t, J = 7.9 Hz, 2H), 8.11 (d, J = 9.2 Hz, 2H), 8.20 (t, J = 7.6 Hz, 2H), 8.65 (s, 2H), 8.74 (d, J = 7.9 Hz, 2H), 8.86 (d, J = 7.9 Hz, 2H). ^{13}C NMR (DMSO-d_6) δ ppm: 52.11; 123.51; 124,00; 125.57; 125.70; 126.78; 129.41; 130.33; 131.27; 135.23; 135.61; 137.06; 149.16; 153.09; 157.06; 158.48; 165.76; 170.06; 176.10.

Langmuir-Blodgett (LB) film deposition

Surface pressure–molecular area (Π-A) isotherms and LB film depositions were conducted in a Nima Tech. Mod. 311D Trough.

For the Langmuir and LB films studies, two different types of solutions were prepared depending on the film studied (**Film 1** or **Film 2**). For the preparation of **Film 1**, solutions

containing 0.50 mg of the [Ru(bpy)$_2$**L**]PF$_6$ and 0.17 mg of stearic acid were dissolved in 1 mL of dichloromethane and then used immediately. For **Film 2**, a solution containing 0.50 mg of [Ru(bpy)$_2$**L**]PF$_6$ and 0.50 mg NH$_4$PF$_6$ was dissolved in 1 ml of dichloromethane and then 2 µL of hydrogen peroxide and 2 µL of hydrochloric acid were added to promote oxidation. This solution was then allowed to react for 1 hour in a closed vessel until the color changed from purple to greenish yellow, indicating the oxidation of the complex. Then, 0.17 mg of stearic acid was added to the oxidized solution.

The concentration of the prepared solutions was calculated considering the mass of the ion pair supposedly formed (complex + stearic acid): **Film 1** was 0.57 mg mL^{-1} (**Film 1** = 950.16 g mol^{-1}) and **Film 2** was 0.74 mg mL^{-1} (**Film 2** = 1233.64 g mol^{-1}).

The Langmuir films were obtained by spreading the investigated complex solution on to ultrapure water subphase (Millipore system, resistivity 18.5 MΩ cm) at 23 °C (± 2 °C). A period of 10 min was allowed for the evaporation of solvent before starting compression. The Π-A isotherms of were recorded with the addition of 50 µL of the solution and a barrier compression velocity of 100 cm^2 min^{-1}. The monolayer stability was evaluated in this same condition by monitoring the change of area at for 3300 s at constant pressure, 33 mN.m^{-1} for **Film 1** and 28 mN.m^{-1} for **Film 2** (Figure S18). Film depositions were accomplished by the addition of 150 µL of the solution, a barrier compression velocity of 100 cm^2 min^{-1}, a constant surface pressure of 33 mNm^{-1} and 28 mNm^{-1}, for **Film 1** and **Film 2**, respectively, and vertical dipping (10 mm min^{-1}). The films were deposited with 20 monolayers, in a type X deposition, in three different substrates (depending on the characterization technique): FTO (for cyclic voltammetry), quartz (for UV-vis spectroscopy) and gold (for IRRAS).

Computational Details

Geometry optimizations were performed at the DFT level using the BP86[41–43] functional, with the Ahlrichs Def2-SVP[44] basis set with Def2-ECP[45] for the ruthenium atom. The auxiliary basis set Def2/J[46] was used for the resolution of identity RI-J[47] approximation; the D3BJ[48,49] dispersion correction was also included in the calculations. All geometries were confirmed as minima in the potential energy surface (PES) by frequencies calculations, which resulted in no imaginary frequency. Single Point energy calculations were made from the optimized geometries using the PBE0[50,51] hybrid functional and same basis set with the RIJCOSX[47] approximation.

Calculations of closed-shell species were made using the Restricted Kohn-Sham (RKS) formalism and open-shell species used the Unrestricted Kohn-Sham (UKS) formalism. All calculations were performed using the Orca 4.1[52,53] suite of quantum chemistry programs.

Crystal structure analysis of $[(\eta^6\text{-}C_6H_6)Ru(L)Cl]\cdot CH_3CH_2OH$

A crystal, *ca* 0.217 x 0.088 x 0.073 mm, under oil, was mounted on a Micro-mount and fixed in the cold nitrogen stream in a Bruker D8 Venture diffractometer equipped with a Photon 100 CMOS detector, Mo–Kα radiation and graphite monochromator. Diffraction intensity data were measured by thin-slice ω- and φ-scans. Data were processed using the APEX3 program[54]. The structure was determined by the direct methods routines in the SHELXS program[55] and refined by full-matrix least-squares methods, on F^2's, in SHELXL[55,56]. The non-hydrogen atoms were refined with anisotropic thermal parameters. The hydrogen atoms of the $[(\eta^6\text{-}C_6H_6)Ru(\mathbf{L})Cl]$ moiety were located in difference maps and were refined freely, except that distance restraints were applied to the H atoms bonded to C(1). The hydrogen atom of the hydroxyl group in ethanol molecule was included in idealized position with U(iso)'s set at

1.5*U(eq) of the parent oxygen atom; the methyl and methylene hydrogen atoms were included in idealized positions with U(iso)'s set at 1.5*U(eq) for the former and 1.2*U(eq) for the latter of the parent carbon atoms. At the conclusion of the refinement, $R_1 = 0.043$ and $R_2 = 0.061$[55,56] for all 4305 reflections weighted w = $[\sigma^2(F_o^2) + (0.0267P)^2 + 5.3726P]^{-1}$ with P = $(F_o^2 + 2F_c^2)/3$; for the 'observed' data only, $R = 0.027$. In the final difference map, the highest peak (*ca* 0.48 eÅ^{-3}) was on the C(13)–C(14) bond. Scattering factors for neutral atoms were taken from the literature[57]. Computer programs used in this analysis were noted above and run through WinGX[58].

ASSOCIATED CONTENT

Supporting Information**.** The supporting information is free of charge on the ACS Publications website at DOI: XXXXXXXX.

Contents. Crystallographic tables and additional ORTEP diagram for complex [(η^6-C_6H_6)Ru(**L**)Cl] and one ORTEP diagram for complex [Ru(bpy)$_2$**L**]PF$_6$. NMR spectra for **L**, [(η^6-C_6H_6)Ru(**L**)Cl] and [Ru(bpy)$_2$**L**]PF$_6$. UV-vis spectroelectrochemistry spectrum of **L**. Molecular orbital diagrams for **L**, **L**•, [(η^6-C_6H_6)Ru(L)Cl], [(η^6-C_6H_6)Ru(L)Cl]$^+$, [(η^6-C_6H_6)Ru(L)Cl]$^-$, [Ru(bpy)$_2$**L**]$^+$, [Ru(bpy)$_2$**L**]$^{2+}$ and [Ru(bpy)$_2$**L**]$^-$; molecular orbital energy tables for **L**, **L**•, [Ru(bpy)$_2$**L**]$^+$, [Ru(bpy)$_2$**L**]$^{2+}$, [Ru(bpy)$_2$**L**]^0, [(η^6-C_6H_6)Ru(L)Cl], [(η^6-C_6H_6)Ru(L)Cl]$^+$ and [(η^6-C_6H_6)Ru(L)Cl]$^-$. Time-stability assay and deposition (FTO) graph for **Film 1** and **Film 2**. CCDC reference number 1888206 refers to compound [(η^6-C_6H_6)Ru(**L**)Cl].

Corresponding Author

*hwin@ufpr.br

ORCID. 0000-0002-1481-5652

Present Addresses

†Max-Planck-Institut für Kohlenforschung, Kaiser-Wilhelm-Platz 1, D-45470 Mülheim an der Ruhr, Germany.

Author Contributions

The manuscript was written with contributions from all the authors. All the authors have given approval to the final version of the manuscript.

REFERENCES

(1)   Sabo-Etienne, S.; Grellier, M. Ruthenium: Inorganic & Coordination Chemistry. In *Encyclopedia of Inorganic Chemistry*; John Wiley & Sons, Ltd: Chichester, UK, 2006. https://doi.org/10.1002/0470862106.ia208.

(2)   Dragutan, I.; Dragutan, V.; Demonceau, A. Editorial of Special Issue Ruthenium Complex: The Expanding Chemistry of the Ruthenium Complexes. *Molecules* **2015**, *20*, 17244–17274. https://doi.org/10.3390/molecules200917244.

(3)   Vos, J. G.; Kelly, J. M. Ruthenium Polypyridyl Chemistry; from Basic Research to Applications and Back Again. *J. Chem. Soc. Dalt. Trans.* **2006**, No. 41, 4869–4883. https://doi.org/10.1039/b606490f.

(4)   Kumar, P.; Gupta, R. K.; Pandey, D. S. Half-Sandwich Arene Ruthenium Complexes: Synthetic Strategies and Relevance in Catalysis. *Chem Soc Rev* **2014**, *43*, 707–733. https://doi.org/10.1039/c3cs60189g.

(5)   Nazarov, A. A.; Hartinger, C. G.; Dyson, P. J. Opening the Lid on Piano-Stool Complexes: An Account of Ruthenium(II)-Arene Complexes with Medicinal Applications. *J. Organomet. Chem.* **2014**, *751*, 251–260. https://doi.org/10.1016/j.jorganchem.2013.09.016.

(6)   Sizova, O. V; Ershov, A. Y.; Ivanova, N. V; Shashko, A. D.; Kuteikina-Teplyakova, A. V. Ru(II) Chloro-Bis(Bipyridyl) Complexes with Substituted Pyridine Ligands : Interpretation of Their Electronic Absorption Spectra. *Russ. J. Coord. Chem.* **2003**, *29* (7), 494–500. https://doi.org/1070-3284/03/2907-0494.

(7)   Habtemariam, A.; Melchart, M.; Fernández, R.; Parsons, S.; Oswald, I. D. H.; Parkin, A.; Fabbiani, F. P. A.; Davidson, J. E.; Dawson, A.; Aird, R. E.; et al. Structure-Activity Relationships for Cytotoxic Ruthenium(II) Arene Complexes Containing N,N-, N,O-, and O,O-Chelating Ligands. *J. Med. Chem.* **2006**, *49* (23), 6858–6868. https://doi.org/10.1021/jm060596m.

(8)   Therrien, B. Functionalised η^6-Arene Ruthenium Complexes. *Coord. Chem. Rev.* **2009**, *253* (3–4), 493–519. https://doi.org/10.1016/j.ccr.2008.04.014.

(9)   Pariyar, A.; Vijaykumar, G.; Bhunia, M.; Dey, S. K.; Singh, S. K.; Kurungot, S.; Mandal, S. K. Switching Closed-Shell to Open-Shell Phenalenyl: Toward Designing Electroactive Materials. *J. Am. Chem. Soc.* **2015**, *137* (18), 5955–5960. https://doi.org/10.1021/jacs.5b00272.

(10)   Mukherjee, A.; Sau, S. C.; Mandal, S. K. Exploring Closed-Shell Cationic Phenalenyl: From Catalysis to Spin Electronics. *Acc. Chem. Res.* **2017**, *50* (7), 1679–1691. https://doi.org/10.1021/acs.accounts.7b00141.

(11)   Sen, T. K.; Mukherjee, A.; Modak, A.; Ghorai, P. K.; Kratzert, D.; Granitzka, M.; Stalke, D.; Mandal, S. K. Phenalenyl-Based Molecules: Tuning the Lowest Unoccupied Molecular Orbital to Design a Catalyst. *Chem. - A Eur. J.* **2012**, *18* (1), 54–58. https://doi.org/10.1002/chem.201103224.

(12)   Mukherjee, A.; Sen, T. K.; Ghorai, P. K.; Mandal, S. K. The Non-Innocent Phenalenyl Unit: An Electronic Nest to Modulate the Catalytic Activity in Hydroamination Reaction. *Sci. Rep.* **2013**, *3* (1), 2821. https://doi.org/10.1038/srep02821.

(13)   Mochida, T.; Torigoe, R.; Koinuma, T.; Asano, C.; Satou, T.; Koike, K.; Nikaido, T. Platinum-Group Chelate Complexes with 9-Hydroxyphenalenone Derivatives: Synthesis, Structures, Spectroscopic Properties and Cytotoxic Activities. *Eur. J. Inorg. Chem.* **2006**, *2006* (3), 558–565. https://doi.org/10.1002/ejic.200500778.

(14)   Das, A.; Ghosh, T. K.; Dutta Chowdhury, A.; Mobin, S. M.; Lahiri, G. K. Electronic Structure and Catalytic Aspects of [(Trpy)(Cl)Ru(L)]n Incorporating Potential Non-Innocent Ligands, L−: 9-Oxidophenalenone and Trpy: 2,2′:6′,2″-Terpyridine. *Polyhedron* **2013**, *52*, 1130–1137. https://doi.org/10.1016/j.poly.2012.06.057.

(15)   Mukherjee, A.; Samuel, P. P.; Schulzke, C.; Mandal, S. K. Main Group Chemistry of 9-Hydroxophenalenone: Syntheses and Structural Characterization of the Alkaline Earth and Zinc Complexes. *J. Chem. Sci.* **2014**, *126* (5), 1581–1588. https://doi.org/10.1007/s12039-014-0692-y.

(16)   Yakuschenko, I. K.; Kaplunov, M. G.; Krasnikova, S. S. Some Metal Complexes of 9-Hydroxyphenalenone as Novel Electron Transporting Materials for OLEDs. *Mol. Cryst. Liq. Cryst.* **2014**, *590* (1), 24–28. https://doi.org/10.1080/15421406.2013.873631.

(17)   Raman, K. V.; Kamerbeek, A. M.; Mukherjee, A.; Atodiresei, N.; Sen, T. K.; Lazić, P.; Caciuc, V.; Michel, R.; Stalke, D.; Mandal, S. K.; et al. Interface-Engineered Templates for Molecular Spin Memory Devices. *Nature* **2013**, *493* (7433), 509–513. https://doi.org/10.1038/nature11719.

(18)   Pal, S. K.; Tham, F. S.; Reed, R. W.; Oakley, R. T.; Haddon, R. C. Synthesis and Characterization of Germanium (IV) and Silicon (IV) Complexes Derived from 9-

Hydroxyphenalenone: X-Ray Crystal and Molecular Structure of Tris-(9-Oxophenalenone)-Germanium (IV) and Silicon (IV) Salts. *Polyhedron* **2005**, *24* (16–17), 2076–2083. https://doi.org/10.1016/j.poly.2005.03.097.

(19) Deun, R. Van; Nockemann, P.; Fias, P.; Hecke, K. Van; Meervelt, L. Van; Binnemans, K. Visible Light Sensitisation of Europium(Iii) Luminescence in a 9-Hydroxyphenal-1-One Complex. *Chem. Commun.* **2005**, *3* (5), 590. https://doi.org/10.1039/b414703k.

(20) Agarwala, H.; Scherer, T. M.; Mobin, S. M.; Kaim, W.; Lahiri, G. K. Bidirectional Non-Innocence of the β-Diketonato Ligand 9-Oxidophenalenone (L$^-$) in [Ru([9]aneS3)(L)(dmso)]^n, [9]aneS3 = 1,4,7-Trithiacyclononane. *Dalt. Trans.* **2014**, *43* (10), 3939-3948. https://doi.org/10.1039/c3dt53069h.

(21) Das, A.; Scherer, T. M.; Mobin, S. M.; Kaim, W.; Lahiri, G. K. 9-Oxidophenalenone: A Noninnocent β-Diketonate Ligand? *Inorg. Chem.* **2012**, *51* (7), 4390–4397. https://doi.org/10.1021/ic300207d.

(22) Kausar, A. Survey on Langmuir–Blodgett Films of Polymer and Polymeric Composite. *Polym. Plast. Technol. Eng.* **2017**, *56* (9), 932–945. https://doi.org/10.1080/03602559.2016.1247282.

(23) Zheng, Q.; Ip, W. H.; Lin, X.; Yousefi, N.; Yeung, K. K.; Li, Z.; Kim, J.-K. Transparent Conductive Films Consisting of Ultralarge Graphene Sheets Produced by Langmuir–Blodgett Assembly. *ACS Nano* **2011**, *5* (7), 6039–6051. https://doi.org/10.1021/nn2018683.

(24) Haddon, R. C.; Rayford, R.; Hirani, A. M. 2-Methyl- and 5-Methyl-9-

Hydroxyphenalenone. *J. Org. Chem.* **1981**, *46* (22), 4587–4588. https://doi.org/10.1021/jo00335a060.

(25)   Caes, B.; Jensen, D. Synthesis and Characterization of 9-Hydroxyphenalenone Using 2D NMR Techniques. *J. Chem. Educ.* **2008**, *85* (3), 413. https://doi.org/10.1021/ed085p413.

(26)   Kljun, J.; Bytzek, A. K.; Kandioller, W.; Bartel, C.; Jakupec, M. A.; Hartinger, C. G.; Keppler, B. K.; Turel, I. Physicochemical Studies and Anticancer Potency of Ruthenium η^6-*p*-Cymene Complexes Containing Antibacterial Quinolones. *Organometallics* **2011**, *30* (9), 2506–2512. https://doi.org/10.1021/om101180c.

(27)   Govindaswamy, P.; Mobin, S. M.; Thöne, C.; Kollipara, M. R. Syntheses and Characterization of η^6-Hexamethylbenzeneruthenium(II)-β-Diketone Complexes: Their Reactions with Mono- and Bidentate Neutral Ligands. *J. Organomet. Chem.* **2005**, *690* (5), 1218–1225. https://doi.org/10.1016/j.jorganchem.2004.11.036.

(28)   Pavlishchuk, V. V.; Addison, A. W. Conversion Constants for Redox Potentials Measured versus Different Reference Electrodes in Acetonitrile Solutions at 25°C. *Inorganica Chim. Acta* **2000**, *298* (1), 97–102. https://doi.org/10.1016/S0020-1693(99)00407-7.

(29)   Oyama, M. Formal Potentials in Non-Aqueous Solvents Part II. Metal Complexes and Fullerenes. *Rev. Polarogr.* **2004**, *50* (2), 87–98. https://doi.org/10.5189/revpolarography.50.87.

(30)   Heijden, M.; Van Vliet, P. M.; Haasnoot, J. G.; Reedijk, J. Synthesis and Characterization of Cis-(2,2′-Bipyridine)(2,2′-Biquinoline) Dichlororuthenium(II) and Its Co-Ordination Chemistry with Imidazole Derivatives. *J. Chem. Soc., Dalton Trans.* **1993**, No. 24, 3675–

3679. https://doi.org/10.1039/DT9930003675.

(31)   Lever, A. B. P. Electrochemical Parametrization of Metal Complex Redox Potentials, Using the Ruthenium(III)/Ruthenium(II) Couple to Generate a Ligand Electrochemical Series. *Inorg. Chem.* **1990**, *29* (6), 1271–1285. https://doi.org/10.1021/ic00331a030.

(32)   Meral, K.; Erbil, H. Y.; Onganer, Y. A Spectroscopic Study of Water-Soluble Pyronin B and Pyronin Y in Langmuir–Blodgett Films Mixed with Stearic Acid. *Appl. Surf. Sci.* **2011**, *258* (4), 1605–1612. https://doi.org/10.1016/j.apsusc.2011.10.008.

(33)   Ferreira, M.; Caetano, W.; Itri, R.; Tabak, M.; Oliveira Jr., O. N. Characterization Techniques to Investigate Molecular-Level Interactions in Langmuir and Langmuir-Blodgett (LB) films. *Quim. Nova* **2005**, *28* (3), 502–510. https://doi.org/10.1590/S0100-40422005000300024.

(34)   Adati, R. D.; Lima, S. A. M.; Davolos, M. R.; Jafelicci, M. Langmuir–Blodgett Films Incorporating an Ionic Europium Complex. *J. Alloys Compd.* **2009**, *488* (2), 595–598. https://doi.org/10.1016/j.jallcom.2009.08.118.

(35)   Dutta, A. K.; Misra, T. N.; Pal, A. J. A Spectroscopic Study of Nonamphiphilic Pyrene Assembled in Langmuir−Blodgett Films: Formation of Aggregates. *Langmuir* **1996**, *12* (2), 459–465. https://doi.org/10.1021/la940678q.

(36)   Pazinato, J.; Hoffmeister, D. M.; Naidek, K. P.; Westphal, E.; Gallardo, H.; Winnischofer, H. Amphiphilic Ruthenium Bipyridine Complex Containing Long-Chain Azopyridine Group and the Mechanism of Electron Transfer in Langmuir-Blodgett Films. *Electrochim. Acta* **2015**, *153*, 574–582. https://doi.org/10.1016/j.electacta.2014.11.136.

(37) Acharya, S.; Parichha, T. K.; Talapatra, G. B. Photophysical Properties of Hexamethoxytriphenylene Mixed with Stearic Acid Assembled in Langmuir–Blodgett Films. *J. Lumin.* **2002**, *96* (2–4), 177–184. https://doi.org/10.1016/S0022-2313(01)00237-X.

(38) Stoll, S.; Schweiger, A. EasySpin, a Comprehensive Software Package for Spectral Simulation and Analysis in EPR. *J. Magn. Reson.* **2006**, *178* (1), 42–55. https://doi.org/10.1016/j.jmr.2005.08.013.

(39) Zelonka, R. A.; Baird, M. C. Benzene Complexes of Ruthenium(II). *Can. J. Chem.* **1972**, *50* (18), 3063–3072. https://doi.org/10.1139/v72-486.

(40) Sullivan, B. P.; Salmon, D. J.; Meyer, T. J. Mixed Phosphine 2,2'-Bipyridine Complexes of Ruthenium. *Inorg. Chem.* **1978**, *17* (12), 3334–3341. https://doi.org/10.1021/ic50190a006.

(41) Perdew, J. P. Density-Functional Approximation for the Correlation Energy of the Inhomogeneous Electron Gas. *Phys. Rev. B* **1986**, *33* (12), 8822–8824. https://doi.org/10.1103/PhysRevB.33.8822.

(42) Perdew, J. P. Erratum: Density-Functional Approximation for the Correlation Energy of the Inhomogeneous Electron Gas. *Phys. Rev. B* **1986**, *34* (10), 7406–7406. https://doi.org/10.1103/PhysRevB.34.7406.

(43) Becke, A. D. Density-Functional Exchange-Energy Approximation with Correct Asymptotic Behavior. *Phys. Rev. A* **1988**, *38* (6), 3098–3100. https://doi.org/10.1103/PhysRevA.38.3098.

(44)   Weigend, F.; Ahlrichs, R. Balanced Basis Sets of Split Valence, Triple Zeta Valence and Quadruple Zeta Valence Quality for H to Rn: Design and Assessment of Accuracy. *Phys. Chem. Chem. Phys.* **2005**, *7* (18), 3297-3305. https://doi.org/10.1039/b508541a.

(45)   Andrae, D.; Häussermann, U.; Dolg, M.; Stoll, H.; Preuss, H. Energy-Adjusted *ab initio* Pseudopotentials for the Second and Third Row Transition Elements. *Theor. Chim. Acta* **1990**, *77* (2), 123–141. https://doi.org/10.1007/BF01114537.

(46)   Weigend, F. Accurate Coulomb-Fitting Basis Sets for H to Rn. *Phys. Chem. Chem. Phys.* **2006**, *8* (9), 1057-1065. https://doi.org/10.1039/b515623h.

(47)   Neese, F.; Wennmohs, F.; Hansen, A.; Becker, U. Efficient, Approximate and Parallel Hartree–Fock and Hybrid DFT Calculations. A 'Chain-of-Spheres' Algorithm for the Hartree–Fock Exchange. *Chem. Phys.* **2009**, *356* (1–3), 98–109. https://doi.org/10.1016/j.chemphys.2008.10.036.

(48)   Grimme, S.; Antony, J.; Ehrlich, S.; Krieg, H. A Consistent and Accurate *ab initio* Parametrization of Density Functional Dispersion Correction (DFT-D) for the 94 Elements H-Pu. *J. Chem. Phys.* **2010**, *132* (15), 154104. https://doi.org/10.1063/1.3382344.

(49)   Grimme, S.; Ehrlich, S.; Goerigk, L. Effect of the Damping Function in Dispersion Corrected Density Functional Theory. *J. Comput. Chem.* **2011**, *32* (7), 1456–1465. https://doi.org/10.1002/jcc.21759.

(50)   Perdew, J. P.; Burke, K.; Ernzerhof, M. Generalized Gradient Approximation Made Simple. *Phys. Rev. Lett.* **1996**, *77* (18), 3865–3868.

https://doi.org/10.1103/PhysRevLett.77.3865.

(51)   Perdew, J. P.; Burke, K.; Ernzerhof, M. Generalized Gradient Approximation Made Simple [Erratum: *Phys. Rev. Lett.* **1996**, *77*, 3865]. *Phys. Rev. Lett.* **1997**, *78* (7), 1396–1396. https://doi.org/10.1103/PhysRevLett.78.1396.

(52)   Neese, F. The ORCA Program System. *Wiley Interdiscip. Rev. Comput. Mol. Sci.* **2012**, *2* (1), 73–78. https://doi.org/10.1002/wcms.81.

(53)   Neese, F. Software Update: The ORCA Program System, Version 4.0. *Wiley Interdiscip. Rev. Comput. Mol. Sci.* **2018**, *8* (1), e1327. https://doi.org/10.1002/wcms.1327.

(54)   APEX3 Bruker AXS Inc. Madison, Wisconsin, USA, **2015**.

(55)   Sheldrick, G. M. A Short History of SHELX. *Acta Crystallogr. Sect. A Found. Crystallogr.* **2008**, *64* (1), 112–122. https://doi.org/10.1107/S0108767307043930.

(56)   Sheldrick, G. M. Crystal Structure Refinement with SHELXL. *Acta Crystallogr. Sect. C Struct. Chem.* **2015**, *71* (1), 3–8. https://doi.org/10.1107/S2053229614024218.

(57)   *International Tables for Crystallography*, Volume C; Ed: Wilson, A. J. C.; Kluwer Academic Publishers, **1992**; pp. 500-502, 219-222, 193-199.

(58)   Farrugia, L. J. WinGX and ORTEP for Windows : An Update. *J. Appl. Crystallogr.* **2012**, *45* (4), 849–854. https://doi.org/10.1107/S0021889812029111.

Synopsis and Table of Contents (TOC)/Abstract Graphic

A new functionalized phenalenyl ligand, named 9-hydroxy-1-oxo-1H-phenalen-5-methyl carboxylate (**L**) and its derivative ruthenium complexes [Ru(bpy)$_2$**L**]PF$_6$ and [(η^6-C$_6$H$_6$)Ru(**L**)Cl] were prepared and characterized by spectroscopic, X-ray diffraction, electrochemical and theoretical methods. Langmuir-Blodgett (LB) films deposited by [Ru(bpy)$_2$**L**]$^{2+/3+}$ species mixed with stearic acid showed electroactive behavior.

For Table of Contents Only